

See discussions, stats, and author profiles for this publication at: <https://www.researchgate.net/publication/216614174>

# Reversible Wettability Changes in Colloidal TiO<sub>2</sub> Nanorod Thin-Film Coatings under Selective UV Laser Irradiation

ARTICLE *in* THE JOURNAL OF PHYSICAL CHEMISTRY C · JANUARY 2008

Impact Factor: 4.77 · DOI: 10.1021/jp0777061

CITATIONS

56

READS

109

10 AUTHORS, INCLUDING:



**Laura Blasi**

Italian National Research Council

28 PUBLICATIONS 186 CITATIONS

SEE PROFILE



**Elvio Carlino**

Italian National Research Council

91 PUBLICATIONS 1,811 CITATIONS

SEE PROFILE



**Liberato Manna**

Istituto Italiano di Tecnologia

318 PUBLICATIONS 16,239 CITATIONS

SEE PROFILE



**Davide Cozzoli**

Università del Salento

137 PUBLICATIONS 5,728 CITATIONS

SEE PROFILE

# Reversible Wettability Changes in Colloidal TiO<sub>2</sub> Nanorod Thin-Film Coatings under Selective UV Laser Irradiation

Gianvito Caputo,<sup>†</sup> Concetta Nobile,<sup>†</sup> Tobias Kipp,<sup>‡</sup> Laura Blasi,<sup>†</sup> Vincenzo Grillo,<sup>§</sup> Elvio Carlino,<sup>§</sup> Liberato Manna,<sup>†</sup> Roberto Cingolani,<sup>†</sup> Pantaleo Davide Cozzoli,<sup>\*,†</sup> and Athanassia Athanassiou<sup>\*,†</sup>

National Nanotechnology Laboratory (NNL) of CNR-INFM, Unità di Ricerca IIT, Distretto Tecnologico ISUFI, via per Arnesano km 5, 73100 Lecce, Italy, Institute of Applied Physics, University of Hamburg, Jungiusstrasse 11, 20355 Hamburg, Germany, TASC-INFM-CNR National Laboratory, Area Science Park–Basovizza, Bld MM, SS 14, Km 163.5, 34012 Trieste, Italy

Received: September 25, 2007; In Final Form: October 25, 2007

We demonstrate the light-induced, reversible wettability of homogeneous nanocrystal-based, thin-film coatings composed of closely packed arrays of surfactant-capped anatase TiO<sub>2</sub> nanorods laterally oriented on various substrates. Under selective pulsed UV laser excitation, the oxide films exhibit a surface transition from a highly hydrophobic and superoleophilic state (water and oil contact angles of  $\sim 110^\circ$  and less than  $\sim 8^\circ$ , respectively) to a highly amphiphilic condition (water and oil contact angles of  $\sim 20^\circ$  and  $\sim 3^\circ$ , respectively). A mechanism is identified according to which the UV-induced hydrophilicity correlates with a progressive increase in the degree of surface hydroxylation of TiO<sub>2</sub>. The observed wettability changes are not accompanied by any noticeable photocatalytic degradation of the surfactants on the nanorods, which has been explained by the combined effects of the intense and pulsed irradiation regime and of the rodlike nanocrystal morphology. The organic ligands on the oxide are instead assumed to rearrange conformationally in response to the light-driven surface reconstruction. The amphiphilic state of the UV-irradiated TiO<sub>2</sub> films is then considered as the macroscopic wetting result of alternating hydrophilic and oleophilic surface domains of nanoscale extension. Upon prolonged storage in the dark, ambient oxygen removes the newly implanted hydroxyl groups from the TiO<sub>2</sub> surfaces and consequently affects again the conformations of ligands such that the films are allowed to recover their native hydrophobic/superoleophilic properties.

## 1. Introduction

The fabrication of functional “smart” surfaces with switchable wetting properties has stimulated intense research efforts due to their importance in both fundamental studies and practical applications, such as in biosensors, microfluidic devices, intelligent membranes, and multifunctional coatings.<sup>1–13</sup>

A class of strategies for the design of solid substrates with dynamically modifiable surface properties exploits geometry and dipole moment changes resulting from conformational transitions in surface-confined organic molecules that respond to externally applied stimuli, such as light irradiation, electrical potential, temperature, solvent, and pH.<sup>1–4,14</sup> Since the wettability modulation achieved with these systems is inherently small (contact angle differences of about  $10^\circ$  are typically measured on flat surfaces), its amplification requires association with nano- and microscale surface roughness.<sup>1–4,14</sup>

Another approach toward more pronounced and switchable wettability changes exploits the reversible property of some semiconductor oxides, such as TiO<sub>2</sub>,<sup>5–12,15</sup> ZnO,<sup>13</sup> WO<sub>3</sub>,<sup>16</sup> and V<sub>2</sub>O<sub>5</sub>,<sup>17</sup> to exhibit increased hydrophilicity upon band gap photoexcitation. Although the related mechanistic aspects are

still a matter of intense debate, this conversion is generally believed to be initiated by photogenerated holes that create oxygen vacancies at the semiconductor surface. These defects are then able to promote dissociative adsorption of atmospheric water, which ultimately leads to an increase in surface hydroxylation. Under dark ambient conditions, a slow recovery of the starting properties occurs as molecular oxygen replaces the UV-grafted hydroxyl moieties.<sup>5–11,13,16–19</sup> These inorganic materials offer clear advantages over stimuli-responsive organic molecules in terms of structural and photochemical stability, low toxicity, and remarkably larger wettability changes (differences as high as  $30\text{--}70^\circ$  in water contact angle values can be observed already for smooth surfaces). The reversible wettability of such photosensitive oxides is crystallographic-facet-dependent<sup>7,8</sup> and can be amplified by suitable morphological texturing of their surfaces. These two aspects can be readily tailored at once by proper synthesis design, eventually providing the basis to achieve superhydrophobic-to-superhydrophilic transitions.<sup>11,13,16,17</sup>

Among the aforementioned materials, TiO<sub>2</sub> has been the most studied one, mainly due to its photocatalytic activity upon UV illumination that has found numerous applications, such as in organic pollutant degradation, in solar energy conversion, and in the deactivation of microorganisms and of malignant cells.<sup>20</sup> The photocatalytic properties of TiO<sub>2</sub> surfaces, combined with their unique capability to convert under UV light from a hydrophobic to a highly amphiphilic state (i.e., simultaneously hydrophilic and oleophilic),<sup>5,6</sup> have paved the way to the development of inorganic TiO<sub>2</sub>-based films with simultaneous

\* To whom correspondence should be addressed. (P.D.C.) Phone: +39 0832 298231. Fax: +39 0832 298238. E-mail: davide.cozzoli@unile.it. (A.A.) Phone: +39 0832 298212. Fax: +39 0832 298238. E-mail: athanassia.athanassiou@unile.it.

<sup>†</sup> National Nanotechnology Laboratory of CNR-INFM.

<sup>‡</sup> University of Hamburg.

<sup>§</sup> TASC-INFM-CNR National Laboratory.

antireflective, antibacterial, self-cleaning, and antifogging behavior.<sup>2,5,6,9,12,21–23</sup> However, the mechanisms of the light-induced properties of TiO<sub>2</sub> still require a deeper insight, essential toward the rational design of functional surfaces for tailored applications, which could take advantage of the photocatalytic activity and the reversible wettability either independently or in combination.

So far, the UV-switchable wettability of TiO<sub>2</sub> has been studied on polycrystalline substrates prepared by sol–gel reactions and subsequent calcination or on micro-/nanostructures grown directly onto substrates.<sup>11,13,16,17</sup> The use of preformed nanoparticles has been restricted only to the fabrication of superhydrophilic films that do not exploit the UV-induced wettability.<sup>12,22,23</sup> Herein, we report on a bottom-up strategy to photoswitchable TiO<sub>2</sub> coatings that exhibit large and reversible wettability changes upon selective UV laser irradiation and dark storage cycles. Our approach relies on the use of surfactant-capped anatase TiO<sub>2</sub> nanorods (NRs) as the building blocks for the fabrication of inorganic/organic thin films. These films are used as coatings for various substrates, such as ITO, silicon, and different polymer surfaces, thus determining the ultimate wettability of these materials. The prepared oxide thin-film coatings consist of closely packed arrays of laterally oriented TiO<sub>2</sub> domains that expose well-defined, light-sensitive crystal facets. Such NR-based films exhibit a reversible surface transition from a highly hydrophobic and superoleophilic state (water and octadecene contact angles of  $\sim 110^\circ$  and less than  $\sim 8^\circ$ , respectively) to a highly amphiphilic condition (water and octadecene contact angles of  $\sim 20^\circ$  and  $\sim 3^\circ$ , respectively) under excitation with pulsed laser light at 355 nm. By combining structural and spectroscopic techniques, a mechanism is identified, according to which the UV-induced hydrophilicity correlates with a progressive increase in the degree of surface hydroxylation of the TiO<sub>2</sub> NR components. Interestingly, the wettability changes are not accompanied by any noticeable photocatalytic degradation of the NR capping surfactants, which can be explained by the joint effects of the intense and periodic irradiation regime and of the nanocrystal morphology. The organic ligands on the oxide are, instead, assumed to undergo conformational rearrangements in response to the light-driven surface reconstruction. The amphiphilic state of the irradiated TiO<sub>2</sub> films is then explained as the macroscopic wetting result of alternating hydrophilic and oleophilic surface domains of nanoscale extension. Upon prolonged storage in the dark, ambient oxygen removes the newly implanted hydroxyl groups from the TiO<sub>2</sub> surfaces, and the ligand conformations are again modified such that the films can recover their native hydrophobic/superoleophilic properties.

## 2. Experimental Section

**2.1. Colloidal Synthesis of TiO<sub>2</sub> Nanocrystals and Film Fabrication.** *Materials.* All chemicals were of the highest purity available and were used as received. Titanium tetraisopropoxide (Ti(OPr<sup>i</sup>)<sub>4</sub> or TTIP, 97%), titanium tetrachloride (TiCl<sub>4</sub>, 99.999%), trimethylamine *N*-oxide dihydrate ((CH<sub>3</sub>)<sub>3</sub>NO·2H<sub>2</sub>O or TMAO, 98%), oleic acid (C<sub>17</sub>H<sub>33</sub>CO<sub>2</sub>H or OLAC, 90%), 1-octadecene (C<sub>18</sub>H<sub>36</sub> or ODE, 90%), oleyl amine (C<sub>17</sub>H<sub>33</sub>NH<sub>2</sub> or OLAM, 70%), polymethylmethacrylate (PMMA, *M*<sub>w</sub> = 120.000), and polystyrene (PS, *M*<sub>w</sub> = 88.000) were purchased from Aldrich. All solvents used were of analytical grade and were also purchased from Aldrich. Water was bidistilled (Millipore Q). Silicon (100) p-type slabs were purchased from Jocom. Indium tin oxide (ITO) substrates were purchased from Praezisions Glas & Optik GmbH.

*Preparation of TiO<sub>2</sub> nanorods.* Unless otherwise stated, all syntheses were carried out under air-free conditions using a standard Schlenk line setup. Organic-capped anatase TiO<sub>2</sub> nanorods with different geometric parameters were synthesized by modified literature protocols.<sup>24,25</sup> TiO<sub>2</sub> NRs with an average diameter of  $\sim 3$ –4 nm and a mean length of  $\sim 25$ –30 nm were obtained by low-temperature TMAO-catalyzed hydrolysis of TTIP.<sup>24</sup> In a typical synthesis, 15 mmol of TTIP was dissolved in 70 g of degassed OLAC, and the resulting solution was then reacted with 5 mL of an aqueous 2 M TMAO solution at 100 °C for 72 h.

Larger TiO<sub>2</sub> NRs, that is, with an average diameter of  $\sim 3$ –5 nm and a mean length up to  $\sim 30$ –40 nm, were synthesized by aminolysis of titanium oleate with oleyl amine.<sup>25</sup> In a typical preparation, 6 g of ODE, 26 mmol of OLAM, and 2 mmol of OLAC were carefully degassed at 120 °C for 20 min, after which the mixture was put under N<sub>2</sub> flow. Then 2 mmol of TiCl<sub>4</sub> was added at 40 °C, and the flask was heated to 290 °C for 30 min.

The TiO<sub>2</sub> NRs were separated from their growing mixture upon 2-propanol addition and were subsequently subjected to repeated cycles of redissolution in toluene and precipitation with acetone to wash out surfactant residuals. Finally, optically clear TiO<sub>2</sub> stock solutions in hexane or toluene were prepared as the precursors for the thin-film coatings. The TiO<sub>2</sub> concentration was determined by inductively coupled plasma atomic emission (ICP-AES) measurements that were performed with a Varian Vista AX spectrometer. The samples for the ICP-AES analyses were prepared by digesting the TiO<sub>2</sub> dried powders in concentrated HNO<sub>3</sub>.

*Preparation of TiO<sub>2</sub> Film Coatings.* Before use, silicon and ITO substrates (1 cm<sup>2</sup>) were immersed into 2-propanol for 10 min; then repeatedly rinsed with acetone; and finally, dried with a nitrogen flow. Polymer-coated substrates were prepared by spin-coating a few drops of a solution of PS or PMMA in either toluene or chloroform at 3000 rpm for 30 s onto silicon or ITO slabs. The thickness of the polymer layer was typically of less than 0.5  $\mu$ m, as measured by a profilometer (Alpha-Step 500, Tencor Instruments).

The TiO<sub>2</sub> NR coatings were fabricated under ambient laboratory conditions as follows: A 500- $\mu$ L volume of a 0.1 M TiO<sub>2</sub> NR stock solution was uniformly spread by dropwise addition onto the surface of liquid water, which half-filled a 250-mL beaker. After the organic solvent was evaporated, a slightly opaque floating TiO<sub>2</sub> film could be recognized on the water surface. At this point, the desired solid substrate (i.e., either bare or polymer-coated silicon or ITO slabs) was gently dipped into the solution and subsequently withdrawn at a rate of 1 cm/min. This sequence was repeated a few times (up to five), as needed. Finally, the TiO<sub>2</sub>-covered substrates were dried with a N<sub>2</sub> flow and kept under vacuum for 3 h.

To evaluate the hydrophobic contribution of OLAC, polycrystalline anatase TiO<sub>2</sub> films on SiO<sub>2</sub>-coated glass slides, prepared according to a literature protocol,<sup>15</sup> were immersed into a dilute OLAC solution (in hexane or toluene) for 24 h in the dark to aid OLAC chemisorption onto the TiO<sub>2</sub> layer. The slabs were gently rinsed with acetone three times to wash out unbound OLAC molecules. The water contact angle increased from about 30° for the uncoated TiO<sub>2</sub> to  $\sim 75^\circ$  for OLAC-coated TiO<sub>2</sub>.

**2.2. Irradiation Experiments.** The TiO<sub>2</sub> coatings were irradiated with the third harmonic wavelength (355 nm) of a pulsed Nd:YAG laser, with a pulse duration of 3 ns, a repetition rate of 10 Hz, and energy density of 5 mJ cm<sup>-2</sup>. The latter value

was measured by an oscilloscope (Tektronik) coupled with an energy meter. The laser spot had a 0.5-cm diameter and was always positioned in the center of the substrate slides to allow for the reproducible identification of the illuminated sample area. The total duration of the irradiation experiments, which was required to detect the largest wettability changes, was found to be 120 min. This period corresponded to 72 000 laser pulses, and hence, to an actual interaction time of UV photons with the TiO<sub>2</sub> samples of only 0.216 ms. Additional irradiation did not affect the film wettability any further.

For a comparison, the TiO<sub>2</sub> coatings were irradiated with a cw UV lamp (with excitation wavelength centered at 365 nm and energy density of 1 mW cm<sup>-2</sup> measured at a distance of 15 cm from the light source). Under these conditions, the organic coating was fully removed in less than ~100 min, as supported by the permanent disappearance of all OLAC infrared absorption bands.

**2.3. Characterization Techniques.** *Transmission Electron Microscopy (TEM).* Low-magnification TEM images of TiO<sub>2</sub> NRs were recorded with a Jeol Jem 1011 microscope operating at an accelerating voltage of 100 kV. Phase-contrast, high-resolution TEM (HRTEM) experiments were performed by using a Jeol 2010F TEM/STEM microscope equipped with YAP UHR large angle detector for HAADF imaging. The microscope was operated at 200 kV, corresponding to an electron wavelength of 0.002 51 nm. The objective lens had a spherical aberration coefficient of  $0.47 \pm 0.01$  mm and, hence, a resolution at optimum defocus of 0.19 nm in HRTEM imaging. The samples for TEM analyses were prepared by dropping a dilute solution of the NRs dissolved in toluene or chloroform onto carbon-coated copper grids and then allowing the solvent to evaporate. Then the grids were immediately transferred to the TEM microscope.

*Scanning Electron Microscopy (SEM).* Low-resolution SEM characterization of TiO<sub>2</sub> coatings deposited onto silicon substrates was performed with a RAITH 150 EBL instrument. Typically, the images were acquired at low accelerating voltages (less than 5 kV).

*Atomic Force Microscopy (AFM).* The topographic features of the TiO<sub>2</sub> NR films were investigated with an atomic force microscope SMENA-B (NT-MDT) working in semicontact mode in air (at 20 °C, relative humidity 30%) using MPP-12120 silicon probes (Veeco) with a resonant frequency of 150 kHz.

*Fourier Transform Infrared Spectroscopy (FT-IR).* Infrared spectroscopy measurements in the 4000–400 cm<sup>-1</sup> spectral range were carried out on TiO<sub>2</sub>-coated silicon substrates using a Bruker Equinox 70 FT-IR apparatus in transmission mode at a resolution of 4 cm<sup>-1</sup>. To compensate for possible changes in the positioning of the samples, all the spectra were normalized to the TiO<sub>2</sub> absorption at 800 cm<sup>-1</sup>. A peak deconvolution procedure was applied to the spectra using the Levenberg–Marquardt method. The accuracy of the fit was estimated by the goodness-of-fit statistical indicator of the software. The error in the calculated peak positions was lower than 10<sup>-5</sup> cm<sup>-1</sup>.

*Raman Spectroscopy.* Raman experiments were performed at room temperature on the TiO<sub>2</sub>-coated substrates by using a diode-pumped solid-state laser (at  $\lambda = 532$  nm) that was coupled into an optical microscope with a 10 $\times$  objective lens, which focused a 8- $\mu$ m light spot onto the sample surface. The Raman scattered light was collected by the same objective and spectrally analyzed by a triple Raman spectrometer (Dilor XY, with a resolution of about 1 cm<sup>-1</sup>) equipped with a Peltier-cooled, deep-depletion CCD detector. Typical acquisition times were on the order of 30–60 s.

*Contact Angle Measurements.* Contact angle characterization was performed on the TiO<sub>2</sub> coatings by the sessile drop method using a CAM200-KSV instrument (equipped with a digital camera for taking magnified images of the microdroplets). Water (bidistilled) and ODE were used as the polar and nonpolar liquids for these tests and dispensed by means of a microsyringe. Typically, the droplet volume was ~3  $\mu$ L. For each sample, the contact angle value was obtained as an average of 5 measurements recorded on different neighboring surface locations. Time-dependent measurements were carried out on TiO<sub>2</sub>-coated substrates before irradiation and immediately after subjecting the samples to a known number of laser pulses, as well as after storing the samples for scheduled time intervals in the dark under ambient conditions (relative humidity 30–40%).

### 3. Results

#### 3.1. Structural Characterization of the TiO<sub>2</sub> Nanorods.

To the purposes of this work, organic-capped TiO<sub>2</sub> nanorods with tailored geometric parameters have been synthesized by employing oleic acid as the promoter of anisotropic growth. After the purification procedures, the NRs are fully dispersible in nonpolar media (such as chloroform, toluene, hexane) due to their hydrophobic organic coating and provide optically clear solutions. Figure 1 illustrates the main morphological–structural details of the as-prepared colloidal TiO<sub>2</sub> nanocrystals. Low-magnification TEM images (panels a, b) show that the samples consist of unidirectionally elongated uniform nanoparticles whose average short and long axis dimensions are tunable between ~3–5 nm and ~10–40 nm, respectively, by adjusting the reaction parameters. Relatively short NRs are characterized by a rodlike profile; longer NRs terminate with an arrowlike shape. High-resolution, phase-contrast TEM investigations along with the relevant fast Fourier transform (FFT) analyses (panels c, d) demonstrate that the NRs are single-crystalline TiO<sub>2</sub> tetragonal anatase nanostructures exhibiting an elongation in the <001> direction, in agreement with the X-ray diffraction pattern of the corresponding NR powders (see Figure S1 in the Supporting Information). Detailed HRTEM examinations of NRs viewed under different zone axes reveal that they expose stepped longitudinal sidewalls dominantly made of crystallographically equivalent (011)/(101) facets, whereas their apexes terminate exclusively with (001) facets. More rarely, (010)-type surfaces can be also observed (panel d). This peculiar morphological–structural arrangement reflects the consecutive alignment of truncated octahedral bipyramidal units, which actually represent equilibrium shape building blocks for TiO<sub>2</sub> anatase, as derived by the Wulff construction and experimentally observed under a variety of solution-phase reaction environments.<sup>20</sup> Under our synthesis conditions, unidirectional nanocrystal growth is believed to be promoted by the stronger adhesion of the OLAC surfactant molecules to the TiO<sub>2</sub> facets associated with the NR longitudinal sidewalls, which lowers their surface energy value below that of other facets.<sup>20,24,25</sup>

#### 3.2. Fabrication and Morphological Characterization of TiO<sub>2</sub> Nanorod Films.

The TiO<sub>2</sub> NR coatings have been fabricated under ambient conditions by transferring the TiO<sub>2</sub> NRs floating at the water/air interface onto the desired substrates by a simple sequential dipping/withdrawal procedure. Different substrates, such as ITO, silicon, PMMA, and PS, have been successfully used with comparable results. The dipping/withdrawal sequence has been repeated up to five times to increase the thickness of the coating, which can thus vary from ~50 to ~300 nm. Subsequently, the samples have been dried



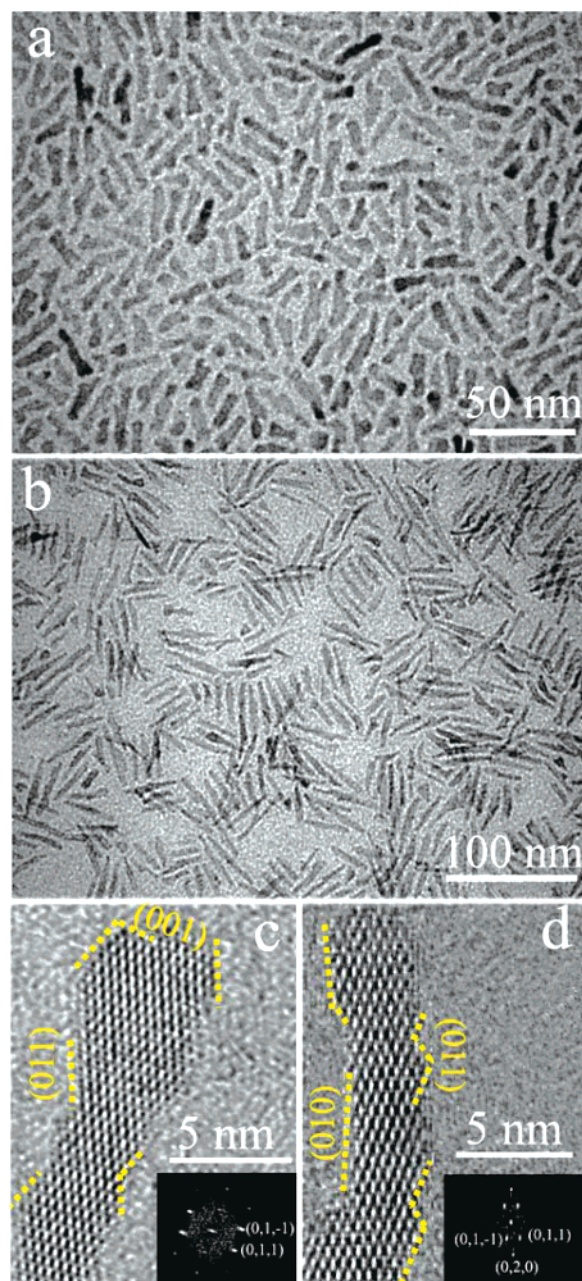


**Figure 1.** (a, b) Low-magnification TEM overview of  $\text{TiO}_2$  nanorods synthesized by the hydrolytic and the nonaqueous approach, respectively. (c, d) HR-TEM images of portions of individual nanorods viewed along their  $[1,0,0]$  zone axes. The dotted yellow lines mark the relevant facets that enclose the nanorods under the observed orientations. In the corresponding insets, FFT analyses of the respective images are reported.

under vacuum at room temperature. As a representative example, Figure 2 demonstrates the surface features of a coating achieved by applying the aforementioned fabrication method to a silicon substrate. SEM and AFM images in panels a and c indicate a rather dense and uniform substrate coverage with almost negligible density of cracks over areas as large as several squared micrometers. The low-magnification SEM overview (panel a) indeed displays homogeneous surfaces without micrometer-scale texturing, whereas the high-resolution inspection (panel b) reveals that the films embody closely packed arrays of NRs, most of which are preferentially accommodated in a roughly parallel orientation with respect to the substrate. Accordingly, AFM analysis (panel c) shows nanometer-scale

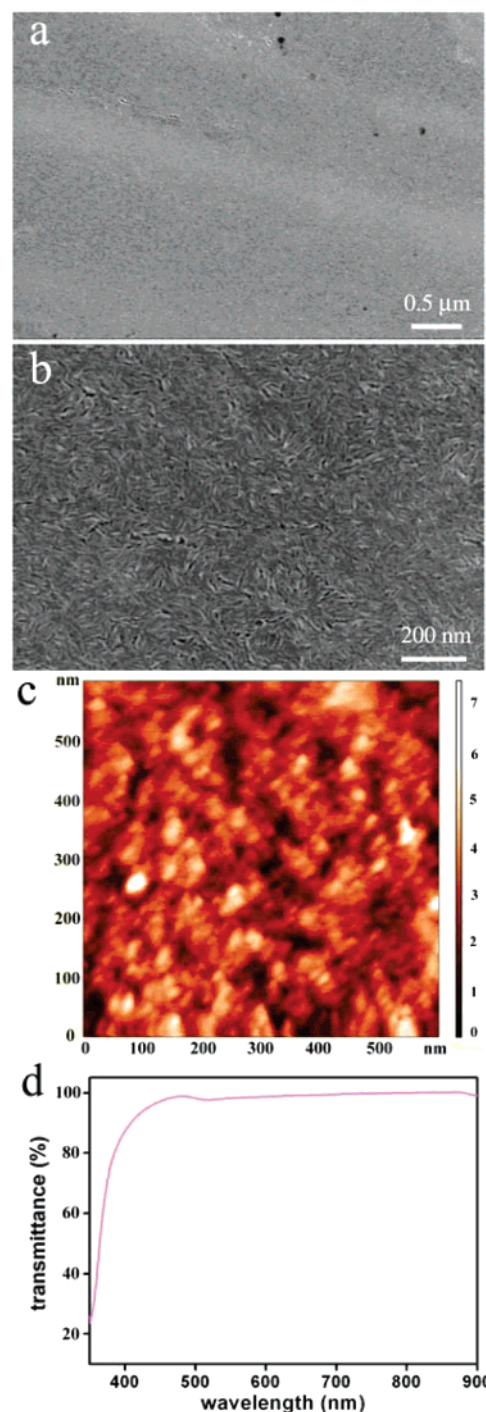


**Figure 2.** (a, b) Representative SEM images of a  $\text{TiO}_2$  thin film ( $\sim 300$  nm in thickness) prepared by dip-coating  $\text{TiO}_2$  nanorods (about 4 nm in width and 40 nm in length) on undoped (100) silicon substrate at low and high magnification, respectively. (c) AFM topographic image corresponding to the same sample in panels a and b. (d) Transmittance spectrum of a  $\sim 300$  nm  $\text{TiO}_2$  film deposited onto ITO. The transmittance at 355 nm is about 30%.

surface roughness, consistent with the organization of NRs in compact, multilayered structures lying almost horizontally relative to the substrate.

The peculiar self-organization adopted by the NRs in the thin-film coatings can be easily understood in terms of surface tension balance, attained during the applied deposition process. When a small volume of a concentrated organic solution of  $\text{TiO}_2$  NRs is spread onto the surface of liquid water and the solvent is allowed to evaporate, hydrophobic interactions among the

surfactant-coated NRs are progressively enhanced due to the increasing TiO<sub>2</sub> concentration in the organic phase. These attractive forces drive the NRs to segregate in closely packed superstructures as a means of decreasing the overall surface energy of the system.<sup>26,27</sup> The rodlike morphology of the TiO<sub>2</sub> nanocrystals promotes their preferential lateral packing, which maximizes the strength of inter-NR interactions while minimizing the TiO<sub>2</sub>/water and the TiO<sub>2</sub>/air interfacial tensions.<sup>27,28</sup> The high cohesive strength among neighboring nanorods guarantees that the obtained superstructures maintain their distinct arrangement intact upon transfer to the desired substrate by the dipping/withdrawal step. The minimum spacing among neighboring NRs should be ultimately dictated by the sterical hindrance of the ligands on the NR facets.

Nevertheless, even assuming that such NR arrangement is repeated across the entire coating thickness, some packing irregularities are expected to be present in the films (e.g., voids due to missing NR building blocks, or NRs deviating from the parallel orientation of the arrays relative to the substrate underneath). Moreover, the surfactant shell around the NRs is likely to be incomplete. Taken together, these arguments suggest that the TiO<sub>2</sub> NR coatings can naturally possess an inner nanoporous structure,<sup>22</sup> which does not, however, affect their optical quality. Indeed, panel d of Figure 2 demonstrates the high transparency of the NR films in the whole visible region. The strong absorption below  $\sim 370$  nm is due to the band gap absorption of TiO<sub>2</sub>. All the NR films present similar surface and optical characteristics independently of the used substrates. These features remain basically unaltered upon UV irradiation.

**3.3. Light-Induced Reversible Wettability Changes.** The wettability properties of the films have been evaluated by water and oil (octadecene) contact angle (WCA and OCA, respectively) measurements following repeated cycles of UV irradiation and prolonged dark storage under ambient conditions. These results, summarized in Figure 3 for a TiO<sub>2</sub> coating on a Si substrate, are similar for all the substrates investigated. The as-prepared films exhibit a stable WCA of  $110 \pm 1^\circ$ , whereas the oil droplet rapidly spreads out, resulting in an OCA of less than  $8.3 \pm 1^\circ$  (panel a). These data undoubtedly indicate that the TiO<sub>2</sub> NR coatings are both highly hydrophobic and superoleophilic. The contact angle values did not change for samples stored in the dark for months, which signified negligible surface contamination by atmospheric species under our lab conditions.

Remarkable wettability changes are induced upon pulsed laser irradiation at  $\lambda_{\text{ex}} = 355$  nm, with a 3-ns pulse duration, and 10-Hz repetition rate, for 120 min (corresponding to a net illumination time of 0.216 ms). The employed UV wavelength guarantees selective band gap excitation of the TiO<sub>2</sub> component, leaving the OLAC coating molecules unaffected. The latter indeed starts absorbing below  $\sim 320$  nm (see Figure S2 in the Supporting Information). At the same time, the low repetition rate of 10 Hz ensures negligible heat production within the film, which may, in fact, influence the kinetics of chemical changes, of molecule adsorption on the TiO<sub>2</sub> surface, or of both.<sup>29,30</sup> Analysis of the evolution of the wetting properties upon increasing the number of pulses (panel a in Figure 3) demonstrates a decrease in the WCA down to  $\sim 20^\circ$ , which proceeds at progressively lower rates. Simultaneously, oil droplets can be observed to spread out over the films at all irradiation stages, indicating constant superoleophilicity (OCA smaller than  $\sim 3$ – $5^\circ$ ). Summarizing, these illumination experiments demonstrate that selective pulsed UV excitation stimulates conversion of TiO<sub>2</sub> NR coatings from a highly hydrophobic and superoleo-

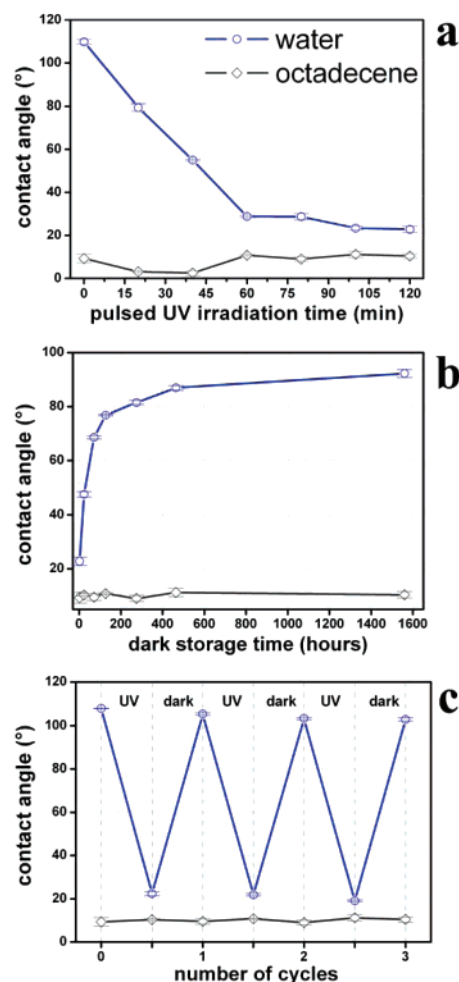


**Figure 3.** (a, b) Time-dependent evolution of the WCA and OCA values on TiO<sub>2</sub> nanorod films under pulsed UV irradiation and dark storage, respectively. The reported OCA values are those measured immediately after the oil droplet deposition. (c) Reversible wettability changes during cyclic alternations of 120-min pulsed UV illumination and 4-month storage in the dark. Note that an overall 120-min duration of the pulsed UV experiment corresponded to an actual irradiation time of 0.216 ms.

philic state to an amphiphilic one, that is, simultaneously highly hydrophilic and superoleophilic.

Subsequent prolonged storage of the samples in the dark (panel b in Figure 3) gradually re-establishes the initial hydrophobic character of the as-prepared TiO<sub>2</sub> NR films. A moderate hydrophobic condition (WCA  $\sim 70^\circ$ ) is already restored during the first 3 days, after which the recovery rate reduces with time so that the original WCA of  $\sim 110^\circ$  is achieved again after  $\sim 4$  months. Again, the above evolution takes place with substantial preservation of the superoleophilicity. The process of the reversible change of the WCA can be carried out over several cycles of irradiation/dark storage (panel c in Figure 3), proving that the NR coatings exhibit excellent reversibility in their wettability properties without being affected by the photochemical fatigue that is, in fact, the main limitation of photoresponsive molecules.<sup>31</sup>

**3.4. Vibrational Spectroscopy.** To gain insight into the mechanism of the UV-light-induced amphiphilicity as well as on its reverse process under dark storage, we have examined the temporal evolution of the characteristic vibrations associated with both the organic and inorganic components of the NR films by FT-IR and Raman spectroscopy. For the sake of clarity, the



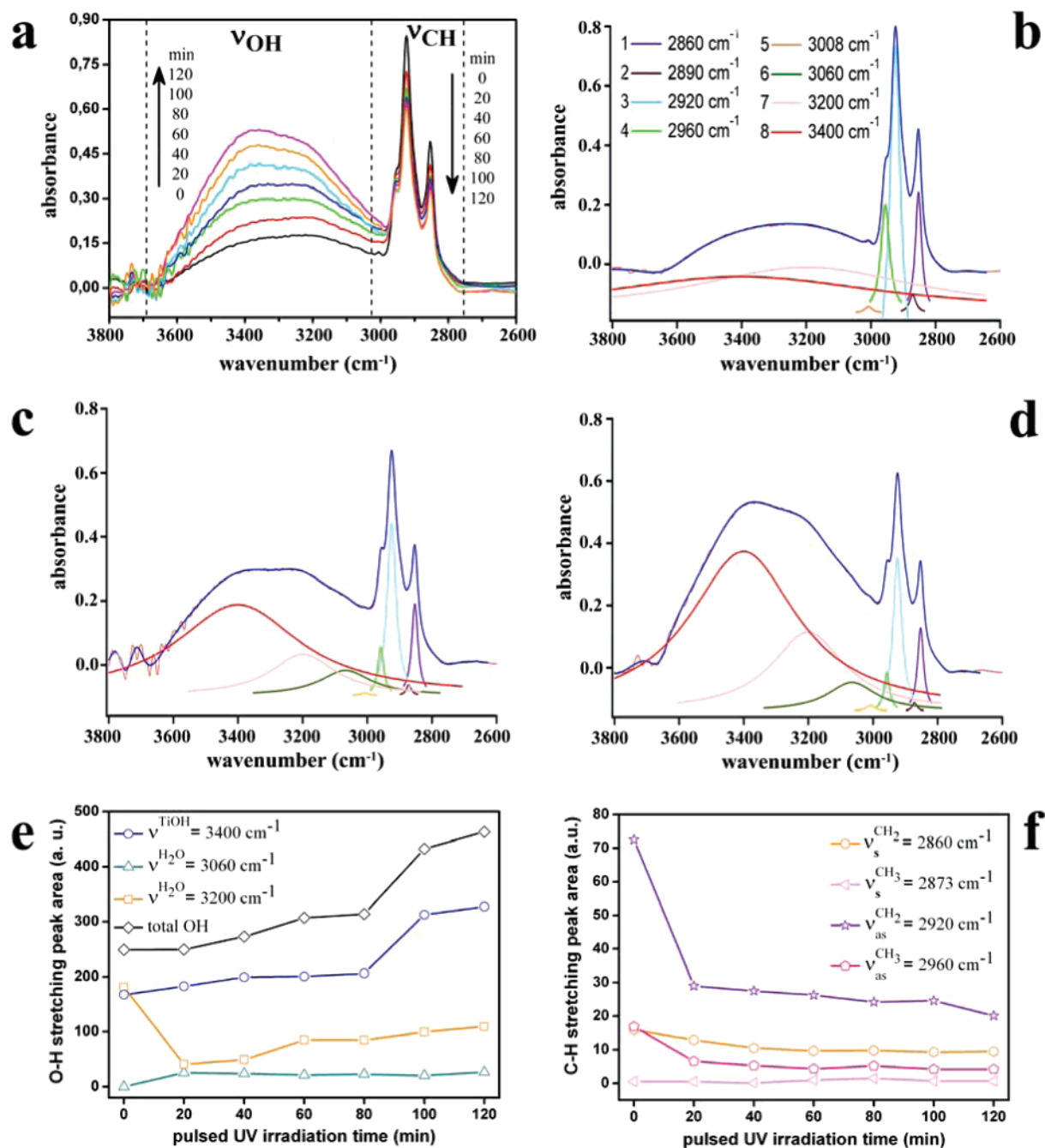


**Figure 4.** Evolution of the TiO<sub>2</sub> nanorod film surface chemistry during a 120-min pulsed UV irradiation: (a) time-dependent FT-IR spectra in the 3800–2600 cm<sup>-1</sup> region; (b, d) Peak deconvolution analysis of the spectra recorded at 0, 40, and 120 min of illumination, respectively; and (e, f) time-dependent changes of the peak area for the relevant O–H stretching and C–H stretching bands, respectively, as derived from the peak deconvolution analyses.

results are reported in separate figures, each one devoted to particular sets of vibrations. In particular, Figures 4 and 5 show the changes in the C–H and O–H stretching signals (in the 3800–2600 cm<sup>-1</sup> region) detected during UV irradiation and dark storage, respectively (these signals are analyzed in detail using peak deconvolution). Figure 6 presents the CO<sub>2</sub><sup>-</sup> stretching and the O–H/C–H bending modes (in the 2000–1200 cm<sup>-1</sup> range). Finally, Figure 7 deals with the TiO<sub>2</sub> lattice phonons that are observable in the 2000–400 cm<sup>-1</sup> interval.

**3.4.1. Spectra of the As-Prepared TiO<sub>2</sub> Films.** In panel a of Figure 4 (graph before irradiation), the FT-IR spectra of as-prepared NR films exhibit the intense antisymmetric and symmetric C–H stretching vibrations of the methylene moieties

in the OLAC alkyl chain at  $\nu(as, CH_2) = 2920$  cm<sup>-1</sup> and at  $\nu(s, CH_2) = 2860$  cm<sup>-1</sup>, respectively. Related spectral deconvolution, presented in panel b, better reveals the asymmetric stretching of the terminal methyl group as a shoulder at  $\nu(as, CH_3) = 2960$  cm<sup>-1</sup>, a minor signal for the corresponding symmetric mode at  $\nu(s, CH_3) = 2872$  cm<sup>-1</sup>, and a very weak but distinct peak for the olefinic =C–H stretching at  $\nu(s, =CH) = 3008$  cm<sup>-1</sup>. The characteristic values of frequency separation for the aforementioned bands suggest the absence of any crystalline-like chain ordering.<sup>32–34</sup> Additionally, it can be noted that the C–H vibrations are superimposed on the low-energy side of a broad O–H stretching band, which consists of the contributions from the signal of terminal titanol groups (i.e.,

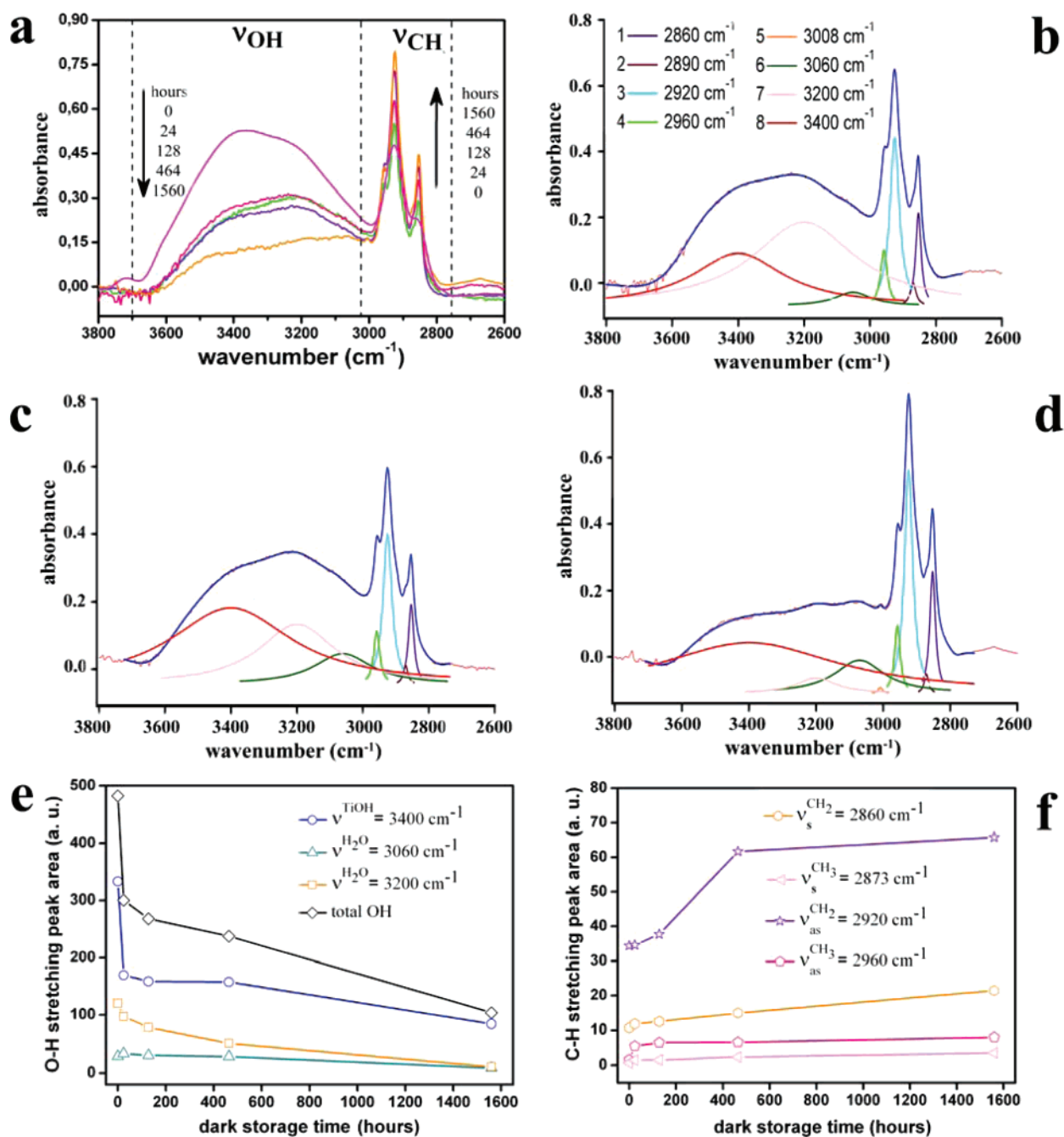


**Figure 5.** Evolution of the TiO<sub>2</sub> nanorod film surface chemistry during dark storage after 120-min pulsed UV irradiation: (a) time-dependent FT-IR spectra in the 3800–2600 cm<sup>-1</sup> region; (b, d) peak deconvolution analysis of the spectra recorded at 128, 468, and 1560 h of dark storage, respectively; and (e, f) time-dependent changes of the peak area for the relevant O–H stretching and C–H stretching bands, respectively, as derived from peak deconvolution analysis.

TiO–H moieties), commonly referred to as dissociatively adsorbed H<sub>2</sub>O, centered at  $\nu(s, \text{TiO–H}) \approx 3400$  cm<sup>-1</sup> and from the signal of hydroxyl groups of molecularly physisorbed H<sub>2</sub>O located at  $\nu(s, \text{H}_2\text{O}) \approx 3200$  cm<sup>-1</sup>.<sup>35–37</sup> As expected, the O–H stretching and bending modes are largely suppressed in the spectrum of the nonhydrolytically prepared TiO<sub>2</sub> NRs due to the involved water-free preparative route (see Figure S3 in the Supporting Information).

Consistently with the above assignments, panel a of Figure 6 (graph before irradiation) shows a weak shoulder for the scissoring (in-plane bending) H<sub>2</sub>O vibrations, located at around  $\delta(s, \text{H}_2\text{O}) \approx 1640$ – $1620$  cm<sup>-1</sup>. The same graph also displays the characteristic antisymmetric and symmetric stretching vibra-

tions of carboxylate anions at  $\nu(\text{as}, \text{CO}_2^-) = 1520$  cm<sup>-1</sup> and at  $\nu(s, \text{CO}_2^-) = 1435$  cm<sup>-1</sup>, respectively. The value of their frequency difference ( $\sim 85$  cm<sup>-1</sup>) indicates that the OLAC ligands are bound to TiO<sub>2</sub> surface by forming mainly chelating bidentate complexes with Ti centers.<sup>38–40</sup> Other signals are identifiable; namely, a shoulder for both the –CH<sub>2</sub>– scissoring and the out-of-plane bending of –CH<sub>3</sub> at  $\delta(s, \text{CH}_2) \approx \delta(\text{as}, \text{CH}_3) \approx 1460$  cm<sup>-1</sup>, as well as several weak peaks for the symmetric bending of –CH<sub>3</sub> at  $\delta(s, \text{CH}_3) \approx 1410$  cm<sup>-1</sup> and for the CH<sub>2</sub>– twisting and the wagging at  $\tau(\text{CH}_2) \approx 1305$  cm<sup>-1</sup> and  $\omega(\text{CH}_2) \approx 1260$  cm<sup>-1</sup>, respectively.

Finally, Figure 7 illustrates the vibrational features associated with the inorganic TiO<sub>2</sub> lattice. In panel a (graph before



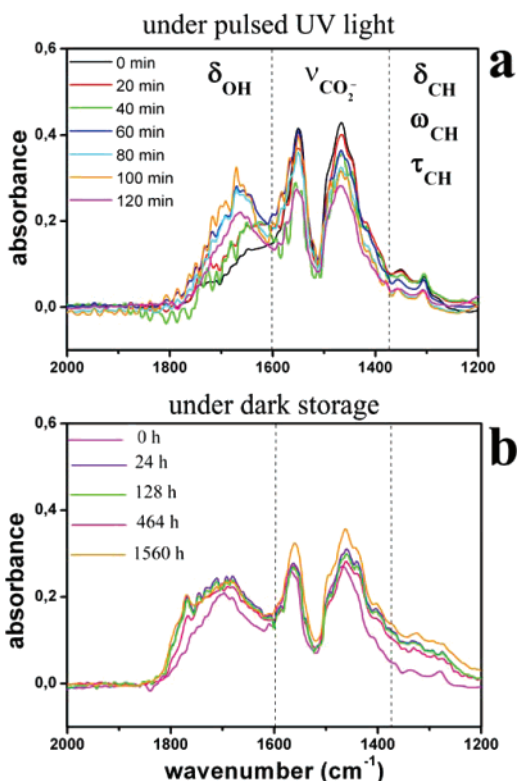


**Figure 6.** Evolution of the TiO<sub>2</sub> nanorod film surface chemistry: time-dependent FT-IR spectra in the 2000–1200 cm<sup>-1</sup> region recorded (a) during 120-min selective UV irradiation and (b) during subsequent dark storage under ambient conditions.

irradiation), an intense and broad increase in absorption can be seen below 1000 cm<sup>-1</sup>, which is due to the infrared-active A<sub>2u</sub> and E<sub>u</sub> longitudinal optical (LO) phonon modes that correspond to stretching- and bending-type vibrations, respectively.<sup>41,42</sup> Surface optical modes are also expected to fall into the same spectral interval, although their exact wavenumber positions are still debated.<sup>42</sup> In panel c of Figure 7, the Raman spectrum of the NR film is in perfect agreement with the pattern for the tetragonal anatase phase, which includes characteristic LO modes, namely E<sub>g</sub> peaks at 151, 200, and 644 cm<sup>-1</sup>, one B<sub>1g</sub> peak at 401 cm<sup>-1</sup>, and unresolved B<sub>1g</sub>/A<sub>1g</sub> peaks at 517 cm<sup>-1</sup>. As a consequence of phonon confinement in nanocrystals, these signals are blue-shifted and exhibit larger and asymmetrically broadened linewidths, as compared to those observed for their bulk counterparts.<sup>43,44</sup>

**3.4.2 Spectra of the UV-Irradiated and Dark-Stored TiO<sub>2</sub> Films.** Upon selective UV irradiation and subsequent storage in the dark, significant modifications in the vibrational spectra are observed. It is worth mentioning that the absolute values of the recorded FT-IR absorbance excursions are almost 2 orders of magnitude higher than those normally detected for organic monolayers adsorbed on planar single crystals or on the outermost exposed grains of compact polycrystalline TiO<sub>2</sub> films.<sup>6,29,45,46</sup> Actually, the present NR films accommodate a remarkably high density of organic species, because they are composed of individually surfactant-capped nanocrystals. Therefore, consistently with the nanoporous nature of the NR films,<sup>22</sup> the evolution of the infrared spectra can be safely considered to reflect average chemical changes occurring throughout the entire oxide coating layer and, hence, on the facets of any of the component NRs, regardless of their location in the films (i.e., either on the surface or in the interior). In addition, control experiments demonstrate that the FT-IR bands of the freshly

prepared, unirradiated TiO<sub>2</sub> NR films remain unaltered (within ±0.005 absorbance unit changes) during dark storage under ambient laboratory conditions for 8–10 months, implying that any contamination due to adsorbed gaseous species from the surrounding atmosphere should be regarded as irrelevant in changing the fundamental chemical features of the involved TiO<sub>2</sub> surfaces.

**3.4.4 Changes in TiO<sub>2</sub> Surface Hydroxylation.** Along the course of the irradiation, one set of signals correlates with the introduction of new chemical functionalities directly onto the TiO<sub>2</sub> surface. In panel a of Figure 4, it appears that the O–H stretching band grows progressively with irradiation pulses, developing shape asymmetry and pronounced humps that disclose the merging of three distinct hydroxyl group species, as revealed by the spectral deconvolution presented in panels b and d. In particular, it can be noted that the pre-existing ν(s, TiO–H) peak at ~3400 cm<sup>-1</sup> exhibits a continuous growth, whereas the pristine ν(s, H<sub>2</sub>O) peak at ~3200 cm<sup>-1</sup> initially decreases and then increases at longer irradiation times (panel e). Significantly, a new band (i.e., absent in the unirradiated films) emerges at ν'(s, H<sub>2</sub>O) ≈ 3060 cm<sup>-1</sup> and soon reaches a stationary intensity. The latter can be assigned to molecularly adsorbed H<sub>2</sub>O being involved in relatively strong H-bondings.<sup>35–37</sup> Other OH-related species, such as bridging hydroxyl moieties or adsorbed noninteracting H<sub>2</sub>O molecules, would usually produce signals at much higher frequencies.<sup>35–37</sup> As evidenced in panel a of Figure 6, the remarkable changes in the O–H stretching region are accompanied by an initial fast growth of the δ(s, H<sub>2</sub>O) mode at around 1660 cm<sup>-1</sup>, followed by its significant decrease at later irradiation times.

The evolution of the OH-related stretching bands upon dark storage of the samples, shown in panels a and d of Figure 5, initially proceeds via a substantial reduction in intensity, which gradually becomes slower over time (panel e). Simultaneously, the development of a rather broad feature centered at 1670–1720 cm<sup>-1</sup> (Figure 6, panel b) may be partly connected to the adjacent carboxylate bands, as will be discussed later. This behavior excludes that the growth of the O–H stretching bands upon UV irradiation could be related to the photocatalytically driven formation of hydroxylated OLAC derivatives (i.e., produced by •OH radical attack), since the latter would be chemically stable under air.

To summarize the changes in TiO<sub>2</sub> surface hydroxylation, upon UV irradiation of the TiO<sub>2</sub> NR films, an increase in overall surface density of hydroxyl moieties on the facets of the NR building blocks occurs. Comparative examination of the kinetic evolution of the O–H stretching and bending bands in Figures 5–6 suggests that H<sub>2</sub>O chemisorption (and hence, dissociation into TiO–H moieties) is enhanced under UV light, proceeding partly at the expense of physisorbed H<sub>2</sub>O and partly by direct H<sub>2</sub>O decomposition on the TiO<sub>2</sub> surface. Both processes would in turn promote further H<sub>2</sub>O accumulation and its stabilization via establishment of H-bondings.<sup>37,47</sup> However, such newly surface-introduced OH species appear to be metastable, because the corresponding bands decline in the dark under air, ultimately tending to restore the initial surface hydroxylation degree.

**3.4.4 TiO<sub>2</sub> Lattice Vibrations.** The UV irradiation and the subsequent dark storage conditions also have an impact on vibrations associated with the inorganic TiO<sub>2</sub> lattice. Panel a in Figure 7 shows that in the region of the infrared-active Ti–O–Ti vibrations, a distinct growth of featureless absorption occurs in the 1100–920 cm<sup>-1</sup> range and below ~700 cm<sup>-1</sup>, which can be interpreted as a selective alteration in the A<sub>2u</sub> and E<sub>u</sub> SO phonons induced by water adsorption, surface hydroxy-

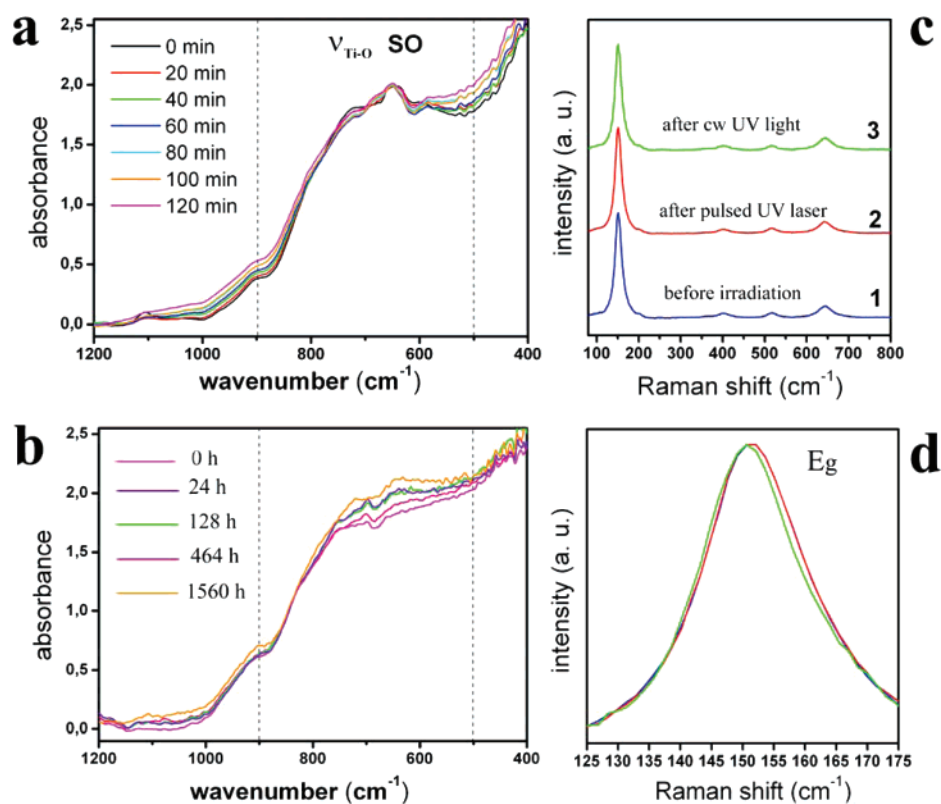


**Figure 7.** Evolution of the TiO<sub>2</sub> nanorod film surface chemistry: (a, b) time-dependent FT-IR spectra in the 1200–400 cm<sup>−1</sup> region recorded during 120-min pulsed UV irradiation and during subsequent dark storage under ambient conditions; (c, d) Raman spectra of the TiO<sub>2</sub> films before (trace 1) and after 120 min irradiation with pulsed UV laser (trace 2) or with cw UV lamp (trace 3). An enlarged view of the E<sub>g</sub> Raman peaks is shown in panel d for the respective cases.

lation, or both.<sup>42</sup> This assignment indeed agrees with the known dependence of SO vibrations on changes in the coordination environment of surface atoms, as well as on variations in the dielectric constant of the medium that immediately surrounds the exposed crystal facets (i.e., air and any adsorbed species in the present case). In addition, subsequent storage in the dark causes some modifications in the spectral features (panel b), which, however, do not resemble a reverse behavior, as compared to that observed under UV. Complementary information on the nature of TiO<sub>2</sub> surface modification is provided by corresponding Raman scattering measurements, because this technique can sensitively probe a number of sample features, such as, for example, local lattice imperfections, nonstoichiometry, crystal strain, and surface relaxation.<sup>43,44,48</sup> Panel c (traces 1, 2) shows that the anatase LO modes remain practically unaffected after UV irradiation. By comparison, if the sample is previously subjected to continuous irradiation with a conventional cw UV lamp, which photocatalytically removes the OLAC ligands (see Figure S4 in the Supporting Information), the associated Raman spectrum exhibits a small but distinct shift in the main E<sub>g</sub> peak as well as a slight band broadening (see trace 3 in panel c and panel d). This result indicates that passivation of the TiO<sub>2</sub> NRs by the OLAC ligands has a stronger influence on relaxation/contraction of the oxide surfaces than the effects produced by the photoinduced hydroxylation process.<sup>48</sup>

**3.4.5 OLAC Ligand Vibrations.** The temporal behavior of the vibrations relative to the OLAC ligands can be studied by analysis of the FT-IR data reported in Figures 4–6. In panels a–d of Figure 4, a sudden decrease in the  $\nu(\text{as, CH}_2)$  and of the  $\nu(\text{s, CH}_3)$  stretching vibrations occurs in the early stages of UV illumination, after which they do not extinguish further.

On the contrary, the  $\nu(\text{s, CH}_2)$  stretching remains almost unaffected over the entire irradiation period. As a consequence, a change in the relative intensity ratio of the above C–H bands is observed (panel f). Moreover, under light, the  $\tau(\text{CH}_2)$  and the  $\omega(\text{CH}_2)$  signals exhibit only a transitory intensity loss, after which they grow even beyond their initial values.

As shown in panel a of Figure 6, the  $\nu(\text{as, CO}_2^-)$  and  $\nu(\text{s, CO}_2^-)$  bands are gradually attenuated under light. The lack of the normally intense and narrow C=O and the broad C–OH stretching signals (which typically are located at 1710 and 1280 cm<sup>−1</sup>, respectively, in un-ionized OLAC) excludes that the CO<sub>2</sub><sup>−</sup> band decrease is caused by protonation of the oleate ligands, ultimately yielding uncharged OLAC or OLAC (or both) molecules having a C=O bound to a protonated titanol, Ti–OH<sub>2</sub><sup>+</sup>, via H-bonding.<sup>38,39</sup> On the basis of the same argument, the formation of short-chain carboxylic acids, which are the primary derivatives of •OH radical-activated oxidative cleavage of OLAC at its double bond,<sup>49,50</sup> can be reasonably ruled out. On the other hand, if the O–H stretching absorbance growth during irradiation were substantially fed by the aforementioned OLAC byproducts, its subsequent decrease upon dark storage could not be accounted for.

Overall, the above-described evolutions of the C–H and –CO<sub>2</sub><sup>−</sup> bands under pulsed UV light are in apparent contrast with the usual abatement kinetics of alkyl carboxylic acids on irradiated TiO<sub>2</sub> surfaces.<sup>49,51</sup> The occurrence of photocatalytically driven degradation of the OLAC capping is further discredited by the results presented in panels a, d, and f of Figure 5 and in panel b of Figure 6, which clearly show that both the C–H stretching and the –CO<sub>2</sub><sup>−</sup> stretching bands recover significantly during dark storage. In addition, the reappearance of the very weak  $\nu(\text{s, =CH})$  peak of OLAC after the intensity

decrease of the overlapped OH stretching band (see graph at storage time  $t = 1560$  h in panels a and d of Figure 5) proves the chemical intactness of the inner C=C double bond. Overall, the fact that major changes in the OLAC signals occur in the first part of the dark storage period, in analogy with the recovery behavior of the OH-related bands, highlights their close correlation with the concomitant decrease in the degree of TiO<sub>2</sub> surface hydroxylation.

The evolution of C–H bending signals in the dark appears to be less straightforward to interpret, because this process does not exhibit a completely inverted trend with respect to that observed under UV irradiation. In fact, the relative intensity ratios of the C–H and CO<sub>2</sub><sup>−</sup> stretching signals in the unirradiated TiO<sub>2</sub> NR films are not completely restored. In the case of the CO<sub>2</sub><sup>−</sup> bands, the original chelating bidentate binding mode of the carboxylate moieties seems to be basically preserved (as judged from the almost unaffected interval between the  $\nu(\text{as, CO}_2^-)$  and  $\nu(\text{s, CO}_2^-)$  frequencies). Nevertheless, minor accentuation of the characteristic spectral features at around 1660–1670 cm<sup>−1</sup> may allow one to presume modifications in the geometrical arrangement of the carboxylate toward a bridging-type complex.<sup>40</sup> A renewed growth of the  $\delta(\text{s, H}_2\text{O})$  band in the same region under dark storage can be excluded by our control experiments, which additionally prove that the recovery of the OLAC bands cannot be due to spontaneous deposition of ambient hydrocarbons.

#### 4. Discussion

In this study, we have presented a bottom-up strategy to photoswitchable TiO<sub>2</sub> surfaces that show large and reversible wettability changes under pulsed laser UV irradiation. We have achieved this goal by fabricating homogeneous TiO<sub>2</sub> thin-film coatings composed of surfactant-capped TiO<sub>2</sub> NRs that are laterally oriented in a closely packed array arrangement on various substrates. These NR-based films generally undergo a surface transition from a highly hydrophobic and superoleophilic state (WCA and OCA of  $\sim 110^\circ$  and  $\sim 8^\circ$ , respectively) to a highly amphiphilic condition (WCA and OCA of  $\sim 20^\circ$  and  $\sim 3^\circ$ , respectively) under selective UV excitation with energy density as low as 5 mJ cm<sup>−2</sup>. Detailed structural, morphological and spectroscopic studies have been performed that allow us to provide an insight into the mechanism, sketched in Figure 8, that is responsible for the observed wettability conversion.

The FT-IR analyses confirm that the colloidal NRs that compose the films are individually passivated by an OLAC shell, being such that the carboxylate groups are directly anchored to the exposed crystal facets, while the alkyl chains protrude outward, assuming disordered orientations. The NRs can also be expected to carry surfactant-free surface areas of nanometer extension, because ligand passivation on nanocrystals is usually incomplete. Titanol groups and adsorbed water already contaminate the facets of the as-synthesized nanocrystals (Figure 8, top image); however, their density can be considered to be very low (especially in the NRs synthesized nonhydrolytically). Actually, the fact that the employed NRs, regardless of the preparative route, are highly soluble in nonpolar solvents demonstrates that the OLAC shell confers them a dominantly hydrophobic character.

The reversible wettability behavior upon cycles of UV laser irradiation/dark storage can be explained by the modifications in the vibrational spectra of the NR films. FT-IR and Raman data jointly prove that the selective band gap excitation of the TiO<sub>2</sub> NR films leads to an increase in the overall surface density of hydroxyl moieties on the facets of the NR that compose the

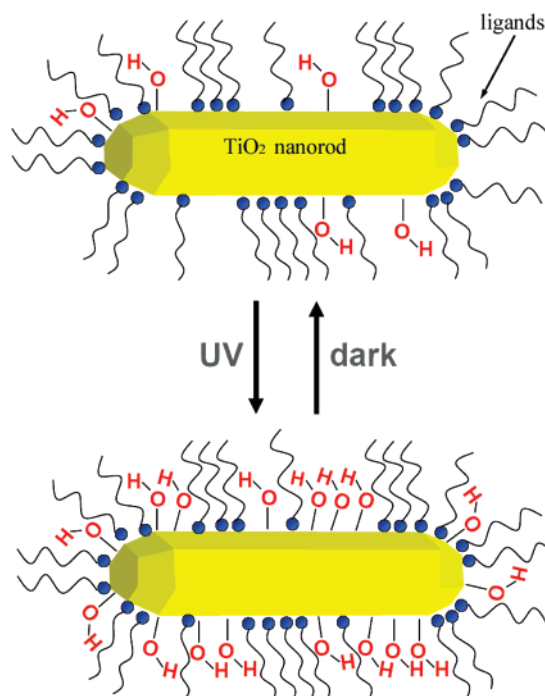


**Figure 8.** Sketch of the mechanism responsible for the reversible wettability changes of the films made of the OLAC-capped TiO<sub>2</sub> nanorods.

films, which are then recovered after subsequent dark storage. Various sets of reversible changes with minor modifications are observed in the chemical–vibrational scenario relative to the OLAC coating. Two main conclusions can be drawn: first, the dynamic hydrophobic-to-hydrophilic transition of the films closely correlates with changes in the degree of TiO<sub>2</sub> hydroxylation;<sup>6,10</sup> and second, the permanent superoleophilicity state and the impossibility to reach a superhydrophilic condition (i.e., WCA = 0°) upon UV irradiation appears to be related to the ubiquitous presence of the nonpolar alkyl chains of the OLAC ligands that are not removed photocatalytically (Figure 8, bottom image). Thus, the possibility to accommodate a substantial density of terminal TiO–H moieties adsorbed in the TiO<sub>2</sub> films actually supports the fact that only a small surface fraction of the as-synthesized NRs is passivated by the OLAC ligands.

The above-described organic surface environment on the as-synthesized NRs provides the freshly deposited films with both superoleophilicity and high hydrophobicity. The latter property is remarkably enhanced as compared to that generally observed on bare TiO<sub>2</sub> surfaces (typical WCA for anatase surfaces is not higher than  $\sim 40$ – $50^\circ$ ).<sup>9,15,52</sup> Such an elevated hydrophobicity can be attributed in part to the intrinsic hydrophobic character of the OLAC coating (note that the WCA for an OLAC monolayer film adsorbed on a polycrystalline TiO<sub>2</sub> film deposited on SiO<sub>2</sub>-coated glass substrates is about  $\sim 75^\circ$ ),<sup>15</sup> and in part to the nanoroughness/nanoporosity of the prepared oxide coatings. Indeed, according to the Cassie–Baxter model developed to describe the wettability of rough surfaces,<sup>53</sup> only partial wetting of such surfaces may occur, due to the trapping of air underneath the water droplet at the recessed regions of the surfaces. In general, the WCA value on a rough surface,  $\theta_r$ , is an average between the value  $\theta_{\text{air}}$ , which the droplet would exhibit on air (i.e.,  $\theta_{\text{air}} = 180^\circ$ ) and the value  $\theta$ , which the droplet would exhibit on the corresponding flat surface. Under these conditions, a rough surface will always yield a higher WCA than the corresponding flat surface, and the WCA value will increase with an increasing degree of roughness.



In the case of our TiO<sub>2</sub> NR films, the WCA value,  $\theta_{\text{nr}}$ , on the nanorough surface is the average among the values  $\theta_{\text{air}}$ , measured on air ( $\theta_{\text{air}} = 180^\circ$ ), the value  $\theta_{\text{TiO}_2}$ , measured on a flat and bare anatase TiO<sub>2</sub> surface ( $\theta_{\text{TiO}_2} = 40\text{--}50^\circ$ ), and the value  $\theta_{\text{OLAC}}$ , measured on a OLAC monolayer ( $\sim 75^\circ$ ). The model is described by the following:

$$\cos(\theta_{\text{nr}}) = f_1 \cos(\theta_{\text{TiO}_2}) + f_2 \cos(\theta_{\text{OLAC}}) + f_3 \cos(\theta_{\text{air}}) \quad (1)$$

where  $f_1$  is the fraction of the liquid drop surface in contact with the TiO<sub>2</sub> surface,  $f_2$  is the fraction of the drop surface in contact with the OLAC layer shell, and  $f_3$  is the fraction of the drop surface in contact with air, and

$$f_1 + f_2 + f_3 = 1 \quad (2)$$

By substituting the above-mentioned approximate contact angle values in eqs 1 and 2, the following equation can be obtained:

$$\cos(110^\circ) = f_1 \cos(45^\circ) + f_2 \cos(75^\circ) + (1 - f_1 - f_2) \cos(180^\circ) \Rightarrow 0.66 = 1.71f_1 + 1.26f_2 \quad (3)$$

From eq 3, it can be derived that the overall fraction of the water droplet that is in contact with the underneath solid substrate (i.e., OLAC-capped TiO<sub>2</sub> film coating) before irradiation cannot exceed  $\sim 50\%$ , with the rest lying on air.

After UV irradiation, the typical contact angle of clean anatase TiO<sub>2</sub> films is commonly reported to be about  $0^\circ$ . The fact that for the present NR films the WCA is not reduced below  $20^\circ$  is attributed to the presence of the nonpolar alkyl chains of the OLAC ligands, which are not photocatalytically degraded under the employed irradiation conditions. At a microscopic level, the alternating distribution of hydrophilic domains (related to the newly introduced TiO–H groups) and of hydrophobic domains (associated with surfactant-protected TiO<sub>2</sub> areas) with nanometer extension (Figure 8, bottom) throughout the porous film structure could give rise to a combined two- and three-dimensional nanocapillary infiltration, allowing water droplets to spread out over the TiO<sub>2</sub> coatings.<sup>5,6,22</sup> If the water droplets are assumed to completely wet the surface of the UV-irradiated films without air being trapped underneath, then the measured WCA value should average the effect of the hydroxylated surface fraction and that of the OLAC-covered surface fraction of the wetted films.

The same argument of complete wetting can be used to explain the behavior of the ODE (oil) droplets. The measured OCA value is very low after the preparation of the films and remains almost unchanged upon both UV irradiation and subsequent storage in the dark. Therefore, throughout the irradiation/dark storage cycles, the surface fractions of the bare, OLAC-coated, and hydroxylated TiO<sub>2</sub> always exhibit an oleophilic character. As a consequence, ODE drops can be expected to penetrate into the nanorough surface of the TiO<sub>2</sub> films, resulting in its complete wetting, as actually observed by us.

Our experiments are consistent with previous mechanistic studies, according to which band gap TiO<sub>2</sub> photoexcitation would induce formation of surface defects (oxygen vacancies) at which ambient H<sub>2</sub>O could favorably compete with O<sub>2</sub> for dissociative adsorption.<sup>5–7,10,19,37,54,55</sup> The specific surface atom arrangements is known to be responsible for the crystallographic-facet-dependence of the light-activated wettability changes.<sup>7</sup> These arguments can be applied to the present TiO<sub>2</sub> NR-based films. Here, owing to the roughly parallel orientation of the NRs with respect to the substrate, the TiO<sub>2</sub> surface that is in contact with the macroscopic liquid droplets, as well as

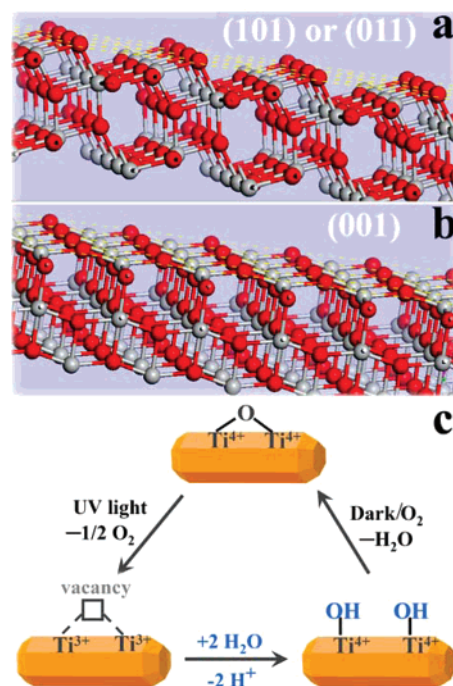


**Figure 9.** (a, b) Atomistic models for (111)/(101) type surfaces and (001) bare surfaces (panels a and b, respectively) in the TiO<sub>2</sub> anatase structure. Oxygen atoms are in red; titanium atoms are in gray. The planes identified by the dotted yellow lines intercept bridging-type oxygen atoms on the outermost exposed atom planes. (c) Sketch of the mechanism of UV-induced hydroxylation of TiO<sub>2</sub> surface areas that are not occupied by the OLAC ligands (for the sake of clarity, the ligands have been omitted).

the walls of the nanochannels between the packed NRs, mainly expose crystallographically equivalent (101)/(011) facets, whereas (001) basal facets represent a minority. The respective features are illustrated in panels a and b of Figure 9. In the anatase structure, low-energy naked (101) and (011) surfaces exhibit a strongly corrugated profile (panel a), in which outmost 2-fold-coordinated O anions (2c-O) are bound to 5-fold-coordinated Ti cations (5c-Ti) (the rest of the structure is made up of lowered 6c-Ti cations and 3c-O anions). On (001) surfaces (panel b), only 5c-Ti atoms are present, which interconnect raised 2c-O and lowered 3c-O anions. In the unirradiated films, H<sub>2</sub>O could adsorb dissociatively only at 5c-Ti sites on (001) surfaces, but it would mainly retain a molecular state on (101)/(011) surfaces.<sup>56,57</sup> The photoinduced increase in TiO<sub>2</sub> hydroxylation could be rationalized by considering that bridging 2c-O sites may be easily removable by the photogenerated holes, in turn leading to highly unstable 4c-Ti<sup>3+</sup> atoms (i.e., oxygen vacancies). Such defect sites are known to possess a strong propensity to be reconstructed by dissociative H<sub>2</sub>O adsorption, resulting in two adjacent TiO–H groups per each healed vacancy.<sup>58,59</sup> The dominance of (101)/(011) facets in our NR films can be thus expected to be a favorable condition for light-induced surface hydroxylation to proceed to a significant extent. Actually, removal of the 2c-O atoms, which are already located in high-energy positions on the (101)/(011) surfaces, could be relatively easier than on (001) facets, since this would cause less geometric distortion. Thus, UV illumination could be described overall as a sort of surface photocorrosion process that involves the topmost exposed atom planes only and creates a high density of suitable sites for chemisorptive H<sub>2</sub>O decomposition.<sup>8</sup> An increasing degree of surface hydroxylation would, in turn, promote adhesion of ordered H<sub>2</sub>O multilayers,<sup>37,47</sup> leading to the formation of hydrophilic domains on the NR

facets. Yet the OH-healed TiO<sub>2</sub> surfaces are neither thermodynamically nor kinetically stable. In fact, once UV irradiation is halted, O<sub>2</sub> substitution for the newly implanted hydroxyl moieties becomes the prevalent chemical reaction under air in the dark. These processes are summarized in panel c of Figure 9. The O–H recovery kinetics observed for the TiO<sub>2</sub> NR films is in good agreement with the aforementioned mechanism. Back-reconstruction proceeds at a comparatively faster rate in the initial period of dark storage, after which further relaxation is slowed down, indicating that the recovery process is complicatedly related to the actual density of UV-reconstructed O–H moieties.<sup>10</sup> The modifications in the TiO<sub>2</sub> SO phonons that have been inferred from our data confirm that the hydrophilic conversion of TiO<sub>2</sub> relies on a genuine surface-confined process involving the topmost exposed atom planes only. Accordingly, the LO modes, which would sensitively reflect both bulk and surface crystal strain fields, remain unaffected, unless the pristine OLAC ligands are removed upon cw UV illumination. This implies that surface stabilization by OLAC binding remains high enough to alleviate or compensate for the surface structural variations associated with the hydroxyl reconstruction process.

The analysis of the time-dependent FT-IR spectra relative to the OLAC ligand provides complementary insight into the origin of the TiO<sub>2</sub> wettability changes. The transition of the TiO<sub>2</sub> films to a highly hydrophilic state does not seem to be accompanied by photocatalytic destruction of the OLAC coating on the NRs under pulsed laser excitation. Neither changes in the extent of TiO<sub>2</sub> hydroxylation involve detachment of the OLAC ligands, although they may slightly affect the anchoring mode of the carboxylate groups on the TiO<sub>2</sub> facets. This is not surprising, owing to the remarkably higher binding affinity of carboxylic acids to TiO<sub>2</sub>, as compared to water.<sup>60</sup> On the other hand, as discussed above, the surface areas of exposed NR facets that are not occupied by the OLAC ligands serve as a suitable ground for the photoinduced introduction of defect sites and, hence, for dissociative H<sub>2</sub>O adsorption (see Figure 8).

We tentatively propose that the FT-IR evolution the OLAC bands taking place during both illumination and dark storage could be attributed to conformational rearrangements of the ligand chains, their anchoring groups, or both that are induced when the density of TiO<sub>2</sub> hydroxylation varies upon photoinduced H<sub>2</sub>O adsorption and desorption under dark. In response to these events, the ligands could be accommodated into substantially different packing configurations on the TiO<sub>2</sub> surface, which would consequently alter the characteristic intensity and frequency of their vibrational modes.<sup>32–34,61–63</sup> Changes in chain-to-chain hydrophobic interactions caused by the UV irradiation could, in turn, affect the back-conformational rearrangements in the dark, thus explaining why the vibrational features that accompany the forward and reverse process may differ to some extent. Such a hypothesis implies preservation of the nonpolar surface microenvironment associated with the alkyl chains of OLAC ligands. This picture would be compatible with the constant superoleophilicity exhibited by the films as well as with their back-conversion to the pristine hydrophobic state upon reduction in the TiO<sub>2</sub> hydroxylation degree in the dark. A confirmation is provided by the behavior exhibited by the TiO<sub>2</sub> coatings that are subjected to cw UV illumination. In this case, as the OLAC capping is photocatalytically destroyed, the WCA is unable to recover above ~60° upon prolonged dark storage (see Figure S4 in the Supporting Information).

The fact that the light-induced wettability changes exhibited by the present NR films are not accompanied by destruction of

the capping ligands on the nanocrystals is a remarkable finding of this study that deserves further discussion. There can be a cooperation of mechanisms able to inhibit the photocatalytic removal of the OLAC molecules, whose presence is essential to guarantee postillumination recovery to the initial hydrophobic state. The peculiar irradiation conditions employed by us should play a fundamental role in this respect.

As mentioned before, pulsed UV laser with a pulse duration of 3 ns and a time interval of about 100 ms between consecutive pulses was used for the irradiation of the NRs. Under such conditions, the photogeneration of a huge number of electron–hole pairs occurs almost simultaneously in only 3 ns, resulting in an extremely high volume density of charge carriers. Such a high number of electron–hole pairs within each NR would considerably increase the probability that either electrons or holes or both migrate to the adjacent NRs and recombine through second-order reactions.<sup>64</sup> After each laser pulse, the carriers can have enough time to recombine (100 ms) so that the next pulse will find the system in a relaxed state. Therefore, under the sufficiently intense laser-pulsed excitation used in this work, electron–hole recombination can occur very efficiently both in the bulk and on the surface of the films so that the production of oxidant radicals that drive the photocatalytic action is greatly suppressed. In this regard, the enhanced charge carrier delocalization that can be expected in NRs as a consequence of their unidirectional shape may further contribute to second-order carrier recombination. This mechanistic hypothesis has been recently supported by experiments on the decay times of photogenerated carriers in TiO<sub>2</sub> nanoparticle films, which demonstrate that photocatalysis can be actually inhibited under the pulsed irradiation regime employed by us.<sup>65</sup>

In most of the cases presented in the literature, photocatalysis has been studied upon irradiating TiO<sub>2</sub> with cw UV lamps so that the generation of the active species needed for photocatalytic action is continuous over time. However, it has been reported<sup>66</sup> that the quantum yields for photo-oxidation in periodically illuminated TiO<sub>2</sub> suspensions are always smaller than those measured under continuous exposure at equivalent average photon absorption rates, since under the former conditions, carrier recombination, which has a characteristic time of about 100 ms, is more efficient. That study is also in agreement with our findings.

Another aspect to consider is that the TiO<sub>2</sub> UV-induced hydrophilicity and photocatalytic action share the same physical origin. Indeed, they are both initiated by band gap photoexcitation of electron–hole pairs, which can either lead to creation of surface oxygen vacancies (available for subsequent hydroxylation) in the former case, initiate radical-based demolition of organics in the latter, or both.<sup>20</sup> However, although the two mechanisms can proceed competitively at the oxide surface, previous studies have pointed out that the hydrophilic conversion should be characterized by a quantum yield value 2–3 orders of magnitude lower than that of the photocatalytic oxidation process.<sup>9,10</sup> From the latter argument, it can be thus expected that even a substantial decrease in the efficiency of photocatalytic reactions may not change the surface hydroxylation process to a significant extent.<sup>10</sup> Our results agree with such an expectation. As a matter of fact, although the pulsed UV photon fluxes provided to the TiO<sub>2</sub> films in our experiments are unable to induce photocatalysis, nevertheless, they suffice to sustain the hydrophilic conversion.

## 5. Conclusions

We have demonstrated a strategy to control the wetting characteristics of different substrates in a reversible manner by

covering them with close-packed films of colloidal TiO<sub>2</sub> NRs. In particular, upon laser pulsed UV irradiation, the NR coatings exhibit a conversion from a highly hydrophobic and oleophilic state to a highly amphiphilic one. This transition is mainly due to an increase in hydroxylation of the TiO<sub>2</sub> surface and can be easily reversed upon prolonged dark storage under ambient conditions. Interestingly, our study proves that suitable irradiation conditions can be selected under which the hydroxylation of the titanium oxide surface is allowed to proceed efficiently without causing photocatalytic destruction of pre-existing passivating ligands. These findings may be useful to suggest additional criteria to engineer light-responsive, oxide-based functional surfaces with tailorable wettability properties.

**Acknowledgment.** This work was supported in part by the European project SA-NANO (Contract No. STRP 013698), by the Italian projects FIRB (Contract Nos. RBLA03ER38 and RBIN048TSE), and by the German Science Foundation via the SFB 508. The authors thank Dr. Roman Krahne for useful discussions and Benedetta Antonazzo for technical assistance in chemical synthesis and irradiation experiments.

**Supporting Information Available:** Powder X-ray diffraction patterns of TiO<sub>2</sub> nanorods, UV-vis absorption spectrum of oleic acid, FT-IR spectra of nonhydrolytically prepared TiO<sub>2</sub> nanorods, and results of irradiation experiments performed with a cw UV lamp. This material is available free of charge via the Internet at <http://pubs.acs.org>

## References and Notes

- (1) Li, X. M.; Reinhoudt, D.; Crego-Calama, M. *Chem. Soc. Rev.* **2007**, 36, 1350–1368.
- (2) (a) Feng, X. J.; Jang, L. *Adv. Mater.* **2006**, 18, 3063–3078. (b) Thompson, T. L.; Yates, J. T. *Chem. Rev.* **2006**, 106, 4428–4453.
- (3) Athanassiou, A.; Lygeraki, M. I.; Pisignano, D.; Lakiotaki, K.; Varda, M.; Mele, E.; Fotakis, C.; Cingolani, R.; Anastasiadis, S. H. *Langmuir* **2006**, 22, 2329–2333.
- (4) Liu, Y.; Mu, L.; Liu, B.; Kong, J. **2005**, 11, 2622–2631.
- (5) Wang, R.; Hashimoto, K.; Fujishima, A.; Chikuni, M.; Kojima, E.; Kitamura, A.; Shimohigoshi, M.; Watanabe, T. *Nature* **1997**, 388, 431–432.
- (6) Wang, R.; Hashimoto, K.; Fujishima, A.; Chikuni, M.; Kojima, E.; Kitamura, A.; Shimohigoshi, M.; Watanabe, T. *Adv. Mater.* **1998**, 10, 135–138.
- (7) Wang, R.; Nobuyuki, S.; Fujishima, A.; Watanabe, T.; Hashimoto, K. *J. Phys. Chem. B* **1999**, 103, 2188–2194.
- (8) Nakajima, A.; Shin-ichi, K.; Watanabe, T.; Hashimoto, K. *J. Photochem. Photobiol., A* **2001**, 146, 129–132.
- (9) Nakajima, A.; Shin-ichi, K.; Watanabe, T.; Hashimoto, K. *Langmuir* **2000**, 16, 7048–7050.
- (10) Sakai, N.; Fujishima, A.; Watanabe, T.; Hashimoto, K. *J. Phys. Chem. B* **2003**, 107, 1028–1035.
- (11) Feng, X.; Zhai, J.; Jiang, L. *Angew. Chem., Int. Ed.* **2005**, 44, 5115–5118.
- (12) Kommireddy, D. S.; Patel, A. A.; Shutava, T. G.; Mills, D. K.; Lvov, Y. M. *J. Nanosci. Nanotechnol.* **2005**, 5, 1081–1087.
- (13) Feng, X.; Feng, L.; Jin, M.; Zhai, J.; Jiang, L.; Zhu, D. *J. Am. Chem. Soc.* **2004**, 126, 62–63.
- (14) Sun, T.; Feng, L.; Gao, X.; Jiang, L. *Acc. Chem. Res.* **2005**, 38, 644–652.
- (15) Miyauchi, M.; Nakajima, A.; Fujishima, A.; Hashimoto, K.; Watanabe, T. *Chem. Mater.* **2000**, 12, 3–5.
- (16) Wang, S.; Feng, X.; Yao, J.; Jiang, L. *Angew. Chem., Int. Ed.* **2006**, 45, 1264–1267.
- (17) Lim, H. S.; Kwak, D.; Lee, D. Y.; Lee, S. G.; Cho, K. *J. Am. Chem. Soc.* **2007**, 129, 4128–4129.
- (18) Sakai, N.; Wang, R.; Fujishima, A.; Watanabe, T.; Hashimoto, K. *Langmuir* **1998**, 14, 5918–5920.
- (19) Sakai, N.; Fujishima, A.; Watanabe, T.; Hashimoto, K. *J. Phys. Chem. B* **2001**, 105, 3023–3026.
- (20) Chen, X.; Mao, S. S. *Chem. Rev.* **2007**, 107, 2891–2959.
- (21) (a) Miyauchi, M.; Nakajima, A.; Hashimoto, K.; Watanabe, T. *Adv. Mater.* **2000**, 12, 1923–1927. (b) Fujishima, A.; Zhang, X. C. *R. Acad. Sci., Ser. IIc: Chim.* **2006**, 9, 750–760.
- (22) Lee, D.; Rubner, M. F.; Cohen, R. E. *Nano Lett.* **2006**, 6, 2305–2312.
- (23) (a) Gan, W. Y.; Lam, S. W.; Chiang, K.; Amal, R.; Zhao, H.; Brungs, M. P. *J. Mater. Chem.* **2007**, 17, 952–954. (b) Zhang, X.-T.; Sato, O.; Taguchi, M.; Einaga, Y.; Murakami, T.; Fujishima, A. *Chem. Mater.* **2005**, 17, 696–700. (c) Zhang, X.; Fujishima, A.; Jin, M.; Emeline, A. V.; Murakami, T. *J. Phys. Chem. B* **2006**, 110, 25142–25148.
- (24) Cozzoli, P. D.; Kornowski, A.; Weller, H. *J. Am. Chem. Soc.* **2003**, 125, 14539–14548.
- (25) Zhang, Z.; Zhong, X.; Liu, S.; Li, D.; Han, M. *Angew. Chem., Int. Ed.* **2005**, 44, 3466–3470.
- (26) Soulantica, K.; Maisonnat, A.; Fromen, M. C.; Casanove, M. J.; Chaudret, B. *Angew. Chem., Int. Ed.* **2003**, 42, 1945–1949.
- (27) Dumestre, F.; Chaudret, B.; Amiens, C.; Respaud, M.; Fejes, P.; Renaud, P.; Zurcher, P. *Angew. Chem., Int. Ed.* **2003**, 42, 5213–5216.
- (28) Sun, B.; Sirringhaus, H. *J. Am. Chem. Soc.* **2006**, 128, 16231–16237.
- (29) Takeuchi, M.; Sakamoto, K.; Martra, G.; Coluccia, S.; Anpo, M. *J. Phys. Chem. B* **2005**, 109, 15422–15428.
- (30) Takeuchi, M.; Martra, G.; Coluccia, S.; Anpo, M. *J. Phys. Chem. C* **2007**, 111, 9811–9817.
- (31) Athanassiou, A.; Sahinidou, D.; Arima, V.; Georgiou, S.; Cingolani, R.; Fotakis, C. *J. Photochem. Photobiol., A* **2006**, 183, 182–189.
- (32) Chia, N. C.; Mendelsohn, R. *J. Phys. Chem.* **1992**, 96, 10543–10547.
- (33) Gao, W.; Dickinson, L.; Grozinger, C.; Morin, F. G.; Reven, L. *Langmuir* **1996**, 12, 6429–6435.
- (34) Srinivasan, G.; Pursch, M.; Sander, L. C.; Muller, K. *Langmuir* **2004**, 20, 1746–1752.
- (35) Nakamura, R.; Ueda, K.; Sato, S. *Langmuir* **2001**, 17, 2298–2300.
- (36) Finnie, K. S.; Cassidy, D. J.; Bartlett, J. R.; Woolfrey, J. L. *Langmuir* **2001**, 17, 816–820.
- (37) Uosaki, K.; Yano, T.; Nihonyanagi, S. *J. Phys. Chem. B* **2004**, 108, 19086–19088.
- (38) Thistlethwaite, P. J.; Hook, M. S. *Langmuir* **2000**, 16, 4993–4998.
- (39) Thistlethwaite, P. J.; Gee, M. L.; Wilson, D. *Langmuir* **1996**, 12, 6487–6491.
- (40) Nara, M.; Torii, H.; Tasumi, M. *J. Phys. Chem.* **1996**, 100, 19812–19817.
- (41) Gonzalez, R. J.; Zallen, R.; Berger, H. *Phys. Rev. B: Condens. Matter Mater. Phys.* **1997**, 55, 7014–7017.
- (42) Warren, D. S.; McQuillan, A. J. *J. Phys. Chem. B* **2004**, 108, 19373–19379.
- (43) Zhang, W. F.; He, Y. L.; Zhang, M. S.; Yin, Z.; Chen, Q. *J. Phys. D: Appl. Phys.* **2000**, 33, 912–916.
- (44) Scepanovic, M. J.; Grujic-Brojcin, M. U.; Dohcevic-Mitrovic, Z. D.; Popovic, Z. V. *Mater. Sci. Forum* **2006**, 518, 101–106.
- (45) Wang, C.; Groenzin, H.; Shultz, M. J. *Langmuir* **2003**, 19, 7330–7334.
- (46) Zubkov, T.; Stahl, D.; Thompson, T. L.; Panayotov, D.; Diwald, O.; Yates, J. T., Jr. *J. Phys. Chem. B* **2005**, 109, 15454–15462.
- (47) Nosaka, A. Y.; Fujiwara, T.; Yagi, H.; Akutsu, H.; Nosaka, Y. *J. Phys. Chem. B* **2004**, 108, 9121–9125.
- (48) Xu, C. Y.; Zhang, P. X.; Yan, L. J. *Raman Spectrosc.* **2001**, 32, 862–865.
- (49) Minabe, T.; Tryk, D. A.; Sawunyama, P.; Kikuchi, Y.; Hashimoto, K.; Fujishima, A. *J. Photochem. Photobiol., A* **2000**, 137, 53–62.
- (50) Tedetti, M.; Kawamura, K.; Narukawa, M.; Joux, F.; Charrière, B.; Sempéré, R. *J. Photochem. Photobiol., A* **2007**, 188, 135–139.
- (51) Allain, E.; Besson, S.; Durand, C.; Moreau, M.; Gacoin, T.; Boilot, J. P. *Adv. Funct. Mater.* **2007**, 17, 549–554.
- (52) Denison, K. R.; Boxall, C. *Langmuir* **2007**, 23, 4358–4366.
- (53) Cassie, A. B. D.; Baxter, S. *Trans. Faraday Soc.* **1944**, 40, 546–551.
- (54) Nosaka, A. Y.; Kojima, E.; Fujiwara, T.; Yagi, H.; Akutsu, H.; Nosaka, Y. *J. Phys. Chem. B* **2003**, 107, 12042–12044.
- (55) Ketteler, G.; Yamamoto, S.; Bluhm, H.; Andersson, K.; Starr, D. E.; Ogletree, D. F.; Ogasawara, H.; Nilsson, A.; Salmeron, M. *J. Phys. Chem. C* **2007**, 111, 8278–8282.
- (56) Vittadini, A.; Selloni, A.; Rotzinger, F. P.; Grätzel, M. *Phys. Rev. Lett.* **1998**, 81, 2954–2957.
- (57) Herman, G. S.; Dohnalek, Z.; Ruzyski, N.; Diebold, U. *J. Phys. Chem. B* **2003**, 107, 2788–2795.
- (58) Zhang, Z.; Bondarchuk, O.; Kay, B. D.; White, J. M.; Dohnalek, Z. *J. Phys. Chem. B* **2006**, 110, 21840–21845.
- (59) Bikondoa, O.; Pang, C. L.; Ithnin, R.; Muryn, C. A.; Onishi, H.; Thornton, G. *Nat. Mater.* **2006**, 5, 189–192.
- (60) Wang, C.; Groenzin, H.; Shultz, M. J. *J. Am. Chem. Soc.* **2005**, 127, 9736–9744.



(61) Lim, H. S.; Han, J. T.; Kwak, D.; Jin, M.; Cho, K. *J. Am. Chem. Soc.* **2006**, *128*, 14458–14459.

(62) Ichimura, K.; Oh, S. K.; Nakagawa, M. *Science* **2000**, *288*, 1624–1626.

(63) Liang, L.; Feng, X.; Liu, J.; Rieke, P. C.; Fryxell, G. E. *Macromolecules* **1998**, *31*, 7845–7850.

(64) Tamaki, Y.; Furube, A.; Murai, M.; Hara, K.; Katoh, R.; Tachiya, M. *Phys. Chem. Chem. Phys.* **2007**, *9*, 1453–1460.

(65) Murai, M.; Tamaki, Y.; Furube, A.; Hara, K.; Katoh, R. *Catal. Today* **2007**, *120*, 214–219.

(66) Cornu, C. J. G.; Colussi, A. J.; Hoffmann, M. R. *J. Phys. Chem. B* **2001**, *107*, 1351–1354.